JACS
JOURNAL OF THE AMERICAN CHEMICAL SOCIETY
Article
pubs.acs.org/JACS

Non-Prussian Blue Structures and Magnetic Ordering of $Na_2Mn^{II}[Mn^{II}(CN)_6]$ and $Na_2Mn^{II}[Mn^{II}(CN)_6]\cdot 2H_2O$

Christopher M. Kareis,[†] Saul H. Lapidus,[‡] Jae-Hyuk Her,[‡,§] Peter W. Stephens,*[,‡,⊥] and Joel S. Miller*[,†]

[†]Department of Chemistry, 315 South 1400 East RM 2124, University of Utah, Salt Lake City, Utah 84112-0850, United States
[‡]Department of Physics & Astronomy, Stony Brook University, Stony Brook, New York 11794-3800, United States
[⊥]Photon Sciences Directorate, Brookhaven National Laboratory, Upton, New York 11973, United States

Supporting Information

ABSTRACT: The aqueous reaction of Mn^{II} and NaCN leads to the isolation of the 3-D Prussian blue analogue (PBA) $Na_2Mn[Mn(CN)_6]\cdot 2H_2O$ (**1·H₂O**), which under careful dehydration forms **1**. **1·H₂O** is monoclinic [$P2_1/n$, a = 10.66744(32) Å, b = 7.60223(23) Å, c = 7.40713(22) Å, β = 92.4379(28)°], while **1** is rhombohedral [$R\bar{3}$, a = 6.6166(2) Å, c = 19.2585(6) Å], and both structures are atypical for PBAs, which are typically face centered cubic. Most notably, the average ∠Mn−N−C angles are 165.3(3)° and 142.4(4)° for **1·H₂O** and **1**, respectively, which are significantly reduced from linearity. This is attributed to the ionic nature of high-spin Mn^{II} accommodating a reduced ∠Mn−N−C to minimize void space. Both **1** and **1·H₂O** magnetically order as ferrimagnets below their ordering temperature, T_c, of 58 and 30 K, respectively, as determined from the average of several independent methods. **1** and **1·H₂O** are hard magnets with 5 K coercive fields of 15 300 and 850 Oe, and remnant magnetizations of 9075 and 102 emu·Oe/mol, respectively. These data along with previous T_c's reported for related materials reveal that T_c increases as the ∠Mn−N−C deviates further from linearity. Hence, the bent cyanide bridges play a crucial role in the superexchange mechanism by increasing the coupling via shorter $Mn^{II}\cdots Mn^{II}$ separations, and perhaps an enhanced overlap.

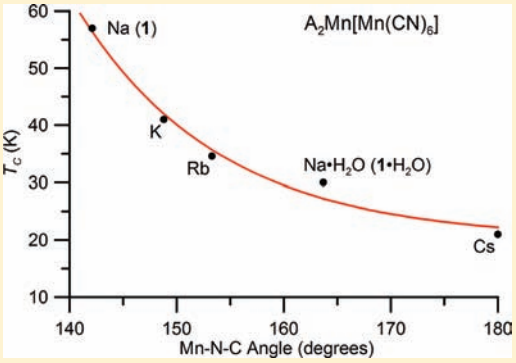

INTRODUCTION

In addition to the numerous hexacyanometalates possessing the face centered cubic (*fcc*) Prussian blue structure that magnetically order,[1−3] a few non-*fcc* magnetically ordered hexacyanometalates, $A_2Mn^{II}[Mn^{II}(CN)_6]$ (A = K, Rb), have been reported.[4] $Cs_2Mn^{II}[Mn^{II}(CN)_6]$, in contrast, possesses the traditional *fcc* Prussian blue structural motif. Magnetic ordering occurs in these materials due to the strong spin coupling between adjacent metal sites via the superexchange interaction[5] between the low-spin $Mn^{II}C_6$ and the high-spin $Mn^{II}N_6$ sites provided by the cyanide ligand. The magnetic ordering temperature, T_c, for this family of ferrimagnets increases as the ∠Mn−N−C decreases as K > Rb > Cs. To test this correlation, the sodium analogue, $Na_2Mn[Mn(CN)_6]$, was sought. Herein, we report the synthesis, structure, and magnetic properties of $Na_2Mn^{II}[Mn^{II}(CN)_6]$ (**1**) and $Na_2Mn^{II}[Mn^{II}(CN)_6]\cdot 2H_2O$ (**1·H₂O**).

EXPERIMENTAL SECTION

$Mn(O_2CMe)_2$ and NaCN were used as purchased from Aldrich. H_2O was purified through a Barnstead "E-pure" water purification system and deoxygenated through distillation under N_2. All other solvents were distilled from the appropriate drying agents under nitrogen before use. All syntheses were performed in an oxygen-free (<1.0 ppm O_2) wet or drybox.

Physical Methods. Infrared spectra were recorded from 400 to 4000 cm^{-1} on a Bruker Tensor 37 spectrometer (±1 cm^{-1}) as KBr pellets and/or Nujol mulls as stated. Thermogravimetric analyses (TGA) were performed at a scan rate of 5 °C/min using a TGA 2050 TA Instruments located in a Vacuum Atmospheres DriLab under nitrogen to protect air- and moisture-sensitive samples. Samples were placed in an aluminum pan and heated at 5 °C/min under a continuous 10 mL/min nitrogen flow.

Magnetic susceptibilities were measured in 1000 Oe applied fields between 5 and 300 K on a Quantum Design MPMS superconducting quantum interference device (SQUID) equipped with a reciprocating sample measurement system, low field option, and continuous low temperature control with enhanced thermometry features, as previously described.[6] Powder samples for magnetic measurements were loaded in gelatin capsules. The temperature dependence of the magnetization was obtained by cooling in zero-field and collecting the data on warming. The remnant magnetization was taken in zero applied field upon warming after cooling in a 5 Oe field. AC susceptibilities were measured at 33, 100, and 1000 Hz. In addition to correcting for the diamagnetic contribution from the sample holder, the core diamagnetic corrections of −120 (**1**) and -146×10^{-6} emu/mol (**1·H₂O**) were used.

Powder X-ray diffraction (PXRD) measurements for Rietveld structure analyses were performed at Beamline X16C of the National Synchrotron Light Source at Brookhaven National Laboratory. The powdered samples were held in an 1.0 mm diameter thin-wall quartz capillary. X-rays of wavelength 0.69711 and 0.69999 Å were

Received: October 18, 2011
Published: December 20, 2011

selected by a Si(111) channel cut monochromator for **1** and **1·H$_2$O**, respectively. Diffracted X-rays were selected by a Ge(111) analyzer and detected by a scintillation counter. The incident intensity was monitored by an ion chamber and used to normalize the measured signal. The TOPAS-Academic program was used to index, solve, and refine the crystal structures.[7−9] Additional powder X-ray diffraction patterns were collected on all samples with a Bruker D8 diffractometer (Cu K$_\alpha$) using Mica (NIST Standard Reference Material 675) as an internal standard.

Na$_2$Mn^{II}[Mn^{II}(CN)$_6$]·*x*H$_2$O (1·H$_2$O). To a 5 mL aqueous solution of Mn(O$_2$CMe)$_2$ (250 mg, 1.44 mmol) was added a 5 mL aqueous solution of NaCN (356 mg, 7.26 mmol). A gray precipitate immediately formed that turned yellow then blue within 15 min. After 4 h of stirring, the blue powder was collected by filtration, washed with 5 × 3 mL of water and 5 mL of Et$_2$O, and dried under vacuum at room temperature for 1 h (yield: 200 mg, 80%). IR (Nujol): υ_{OH} 3608 (m), 3536 (m), υ_{CN} 2079 (s), 2040 (s), υ_{OH} 1621 (s) cm^{-1}.

Na$_2$Mn^{II}[Mn^{II}(CN)$_6$] (1). In a typical experiment, ∼100 mg of **1·H$_2$O** was placed into a vial within a vacuum oven at room temperature. The temperature was increased by 10 °C every 30 min until reaching 110 °C, and then held at 110 °C for 8 h. During this time, the color of the solid went from the dark blue characteristic of **1·H$_2$O** to a dark green characteristic of A$_2$Mn[Mn(CN)$_6$] (A = K, Rb). IR (Nujol): υ_{CN} 2046 (s), 2025 (wsh) cm^{-1}.

■ RESULTS AND DISCUSSION

The aqueous reaction of NaCN and Mn(O$_2$CMe)$_2$ led to the isolation of Na$_2$Mn[Mn(CN)$_6$]·*z*H$_2$O (**1·H$_2$O**) that exhibits two sharp υ_{OH} and υ_{CN} absorptions at 3608 and 3536, and 2079 and 2040 cm^{-1}, respectively. Unlike other Mn^{II} Prussian blue analogues, the υ_{CN} absorptions for **1·H$_2$O** are of equal intensity and result from the water molecules coordinating to the included sodium atoms creating two separate environments experienced by each cyanide. Dehydration of **1·H$_2$O** to form the desired Na$_2$Mn[Mn(CN)$_6$] results in the disappearance of the υ_{OH} absorption and the formation of a single, strong υ_{CN} absorption at 2046 cm^{-1}. The υ_{CN} values are in accord with 2058, 2064, and 2073 cm^{-1} observed for A$_2$Mn[Mn(CN)$_6$] (A = K, Rb, Cs), while the υ_{OH} absorption suggests the presence of water.

Thermal Properties. The thermogravimetric analysis (TGA) trace for **1·H$_2$O** shows it to be thermally stable with respect to weight loss below 60 °C. Water is lost in the range of 60−210 °C, and the amount varies slightly between samples. A typical sample has a 17.7% weight loss corresponding to *z* = 3.74 (Figure 1). This *z* value is greater than what was determined by PXRD analysis (vide infra), forcing further investigation into other components possibly being lost. Detailed mass spectral analysis of the off gases from heating the samples shows evolution of CN by peaks at 27 and 28 *m*/*z*. However, depending on the heating rate, the region in which the −CN peaks are observed varies. Heating from 5 to 550 °C at of 5 °C/min shows CN loss below 100 °C. However, when **1·H$_2$O** is heated slowly (0.5 °C/min) from 5 to 550 °C, CN was only detected above 110 °C along with water. This heating procedure gave the most consistent results. This combination of H$_2$O/CN loss led to the use of *z* = 2 obtained from the structure determination (vide infra) in magnetic calculations, as it was the most consistent.

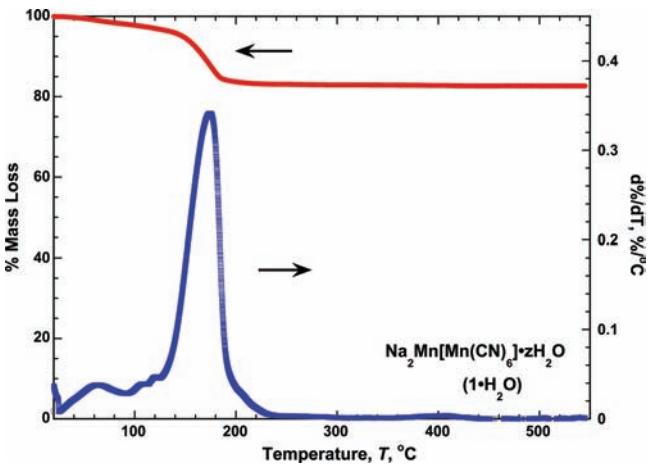

Figure 1. TGA trace for **1·H$_2$O**. H$_2$O was lost between 60 and 210 °C, while CN was lost above 100 °C.

Structure. Both **1** and **1·H$_2$O** were successfully indexed, and space groups of $R\bar{3}$ and $P2_1/n$ were tentatively assigned, respectively. The structures of **1** and **1·H$_2$O** were solved from the synchrotron powder diffraction data by simulated annealing, confirming the space group selection. From this initial structure solution, the structure was successfully refined (Figure 2). These measurements do not clearly distinguish the orientation of the cyano groups; they were assigned from the nearest Mn distance. The crystallographic data for **1** and **1·H$_2$O** are summarized in Table 1. The monoclinic unit cell of **1·H$_2$O** and the rhombohedral unit cell for **1** differ from the cubic *fcc* cells previously reported for Prussian blue structured materials. However, the monoclinic cell has been recently established for A$_2$Mn^{II}[Mn^{II}(CN)$_6$] (A = K, Rb),[4] as well as KMn^{II}[Fe^{III}(CN)$_6$],[10a] and Na$_{1.52}$K$_{0.04}$Co[Fe(CN)$_6$]$_{0.89}$·3.9H$_2$O is reported to have monoclinic and rhombohedral unit cells,[10b] respectively, although the structures of these latter two compounds have not been reported.

Structure of Na$_2$Mn^{II}[Mn^{II}(CN)$_6$]·2H$_2$O, 1·H$_2$O. Na$_2$Mn^{II}[Mn^{II}(CN)$_6$]·2H$_2$O (**1·H$_2$O**) has the same structure at both 16 K and at room temperature, except for a 1.66% volume contraction. This structure is composed of six C-bound cyanides to a Mn(II) ion with an average Mn−C distance of 1.926(6) Å at 16 K, Figure 3a, and a Jahn−Teller distortion is not evident. The other Mn(II) bonds to 6 N's with a Mn−N bond length of 2.264(4) Å at 16 K, Figure 3b. For comparison, the Mn^{II}−C bond distances vary between 1.91 and 1.98 Å for Na$_4$[Mn(CN)$_6$]·10H$_2$O,[11a,b] 1.90 and 2.01 Å for K$_2$Mn[Mn(CN)$_6$], and 1.90 and 1.97 Å for Rb$_2$Mn[Mn(CN)$_6$], respectively.[4] Likewise, the Mn−N distances are comparable to 2.21, 2.18, 2.22, and 2.23 Å reported for Na$_4$[Mn(CN)$_6$]·10H$_2$O, NaMn[Cr(CN)$_6$],[11c] K$_2$Mn[Mn(CN)$_6$], and Rb$_2$Mn[Mn(CN)$_6$].[4] This difference in bond lengths is assigned to the C-bound low-spin Mn^{II}, and N-bound high-spin Mn^{II}, respectively. The Mn−C−N angles of 174.6(7)°, 176.0(8)°, and 177.7(7)° (average = 176.1°) are near linearity, as expected. However, the Mn−N−C angles of 162.2(5)°, 162.6(6)°, and 171.0(7)° (average = 165.3°) deviate substantially from linearity, and while an unexpected result for a Prussian blue structured material, it is in accord with that observed for A$_2$Mn[Mn(CN)$_6$] (A = K, Rb), which average 148.8° and 153.3°, respectively.[4]

Each cyanide bridges a low- and a high-spin Mn^{II} ion to form a 3-D framework structure with void spaces occupied by Na$^+$ and water (Figure 4). The Mn^{II}···Mn^{II} separation average 5.33 Å that is slightly greater than that observed for A$_2$Mn[Mn(CN)$_6$] [A = K (5.09), Rb (5.19 Å)].[4] As a consequence, MnC$_6$ (a) and MnN$_6$ (b) occur in alternating rows and have their octahedra twisted with respect to each other (Figure 4a), but do not tilt as observed for A$_2$Mn[Mn(CN)$_6$] (A = K, Rb).[4]

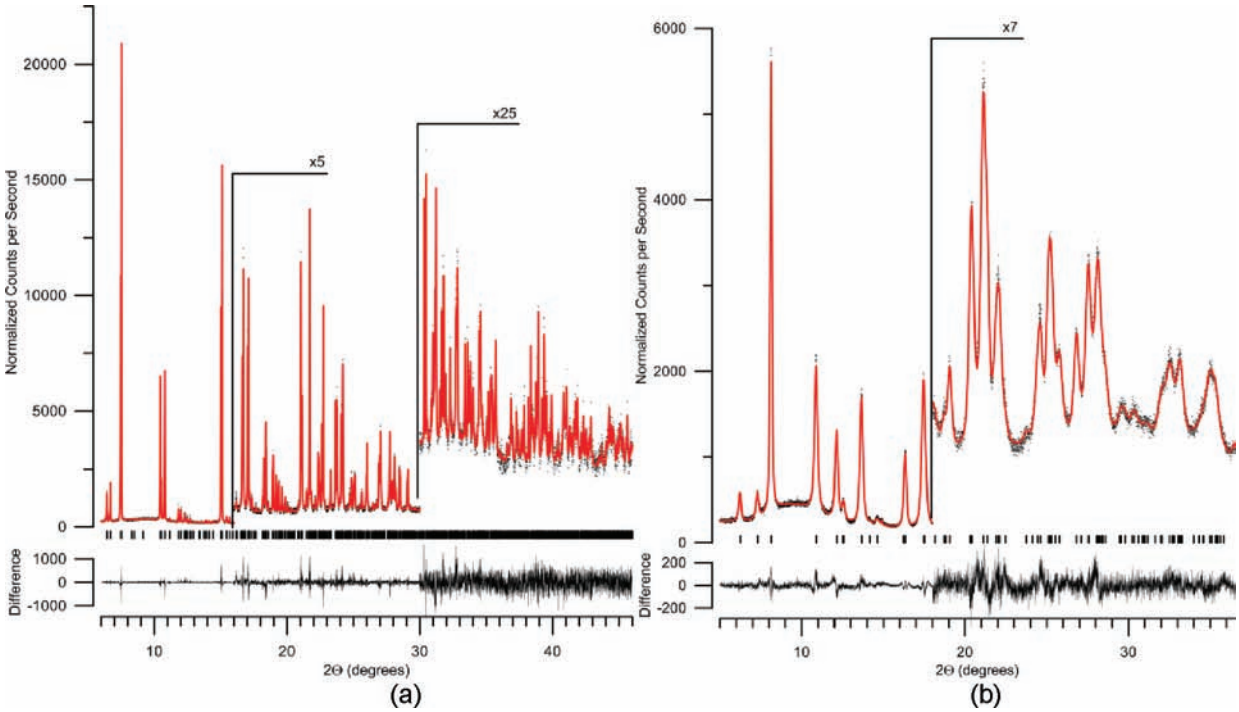

Figure 2. High-resolution synchrotron powder diffraction data (dots) and Rietveld fit (line) of the data for the structure of $Na_2Mn[Mn(CN)_6]\cdot 2H_2O$, **1·H₂O** (a), and room-temperature structure of $Na_2Mn[Mn(CN)_6]$, **1** (b). The lower traces for each plot are the differences, measured − calculated, plotted to the same vertical scale.

Table 1. Summary of Crystallographic Parameters for $Na_2Mn[Mn(CN)_6]\cdot 2H_2O$ (1·H₂O) and $Na_2Mn[Mn(CN)_6]$ (1)

	$Na_2Mn[Mn(CN)_6]\cdot 2H_2O$, **1·H₂O**	$Na_2Mn[Mn(CN)_6]\cdot 2H_2O$, **1·H₂O**	$Na_2Mn[Mn(CN)_6]$, **1**
	monoclinic	monoclinic	rhombohedral
MW, g/mol	171.99	171.99	155.99
a, Å	10.66744(32)	10.62816(32)	6.6166(3)
b, Å	7.60223(23)	7.52341(23)	6.6166(3)
c, Å	7.40713(22)	7.38769(22)	19.2585(9)
α, deg	90	90	90
β, deg	92.4379(28)	92.4366(28)	90
γ, deg	90	90	120
V, Å^3	600.148(31)	590.19(3)	730.17(9)
Z	4	4	6
space group	$P2_1/n$	$P2_1/n$	$R\bar{3}$
ρ_{calc}, g/cm^3	1.903	1.936	2.128
R_{wp}[a,b]	7.88	7.219	3.99
R_{exp}[b,c]	4.60	3.875	3.13
T, K	293	15	293
GOF, R_{wp}/R_{exp}	1.71	1.86	1.27
CCDC no.	848212	848213	848211

[a] $R_{wp} = (\sum_i w_i(y_i^{calc} - y_i^{obs})^2)/(\sum_i w_i(y_i^{obs})^2)^{1/2}$. [b] y_i^{calc} and y_i^{obs} are the calculated and observed intensities at the ith point in the profile, normalized to monitor intensity. The weight w_i is $1/\sigma^2$ from the counting statistics, with the same normalization factor. N is the number of points in the measured profile minus the number of parameters. [c] $R_{exp} = (N)/(\sum_i w_i(y_i^{obs})^2)^{1/2}$.

The Na^+ ions interact with eight cyanides with Na−N and Na−C distances that range from 3.34 to 4.51 Å. Each Na^+ interacts with two water molecules with Na−O distances of 2.43 and 2.57 Å. The Na^+−water interactions form a 1-D zigzag chains that interpenetrate the 3-D $Mn[Mn(CN)_6]$ lattice, Figure 5.

Structure of $Na_2Mn^{II}[Mn^{II}(CN)_6]$ (1). The structure of $Na_2Mn^{II}[Mn^{II}(CN)_6]$ is composed of six C-bound cyanides to a Mn(II) ion with a Mn−C distance of 1.949(4) Å (Figure 3c) and Mn−N distance of 2.263(4) Å (Figure 3d). Again, this difference in bond lengths is assigned to the C-bound low-spin Mn^{II}, and N-bound high-spin Mn^{II}, respectively, in accord with the discussion for **1·H₂O**. The Mn−C−N and Mn−N−C angles are 167.0(4)° and 142.4(4)°, respectively, and both deviate from linearity. Each cyanide bridges a low- and a high-spin Mn^{II} ion to form a 3-D framework structure (Figure 4b). The $Mn^{II}\cdots Mn^{II}$ separations are 4.99 Å, and due to the nonlinear ∠Mn−C−N and ∠Mn−N−C angles, this separation is less than that observed for **1·H₂O** and $A_2Mn[Mn(CN)_6]$ [A = K (5.09), Rb (5.19 Å)].[4] As a consequence, MnC_6 (a) and MnN_6 (b) octahedra occur in alternating rows and are canted

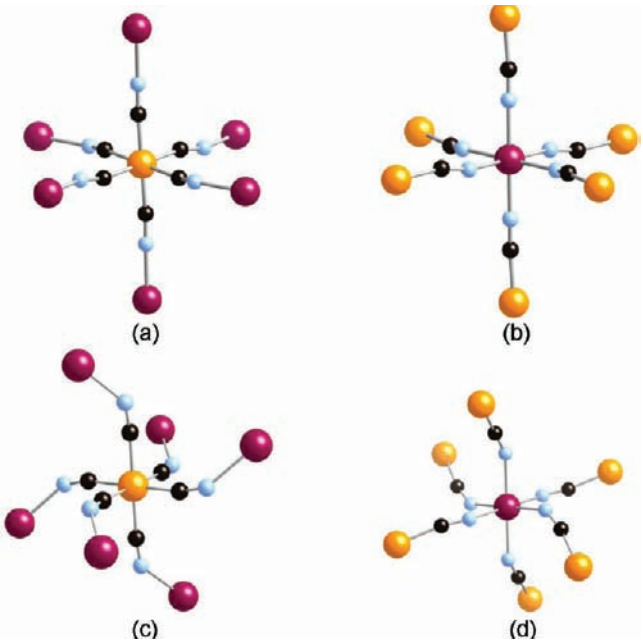

Figure 3. $Mn(CNMn)_6$ (a,c) and $Mn(NCMn)_6$ (b,d) octahedral coordination for **1·H₂O** (a,b) and **1** (c,d), respectively. [Low-spin ($S = 1/2$) Mn^{II} is orange; high-spin ($S = 5/2$) Mn^{II} is maroon; C is black; and N is light blue.]

with respect to each other (Figure 4b), but do not tilt as observed for $A_2Mn[Mn(CN)_6]$ (A = K, Rb).[4]

In contrast to a cubic Prussian blue structural motif where the void spaces are defined by the cubic framework arrangement of atoms arising from covalent M−CN and M′−NC bonding leading to linear ∠M−CN−M′ angles, the less covalent Mn^{II} (more ionic)[12] can accommodate a reduced ∠M−CN−M′, which was induced from the increasing electrostatic interactions that increase with decreasing cation size ($Cs^+ > Rb^+ > K^+ > Na^+$), and minimizes void space, as occurs. Similarly, bent cyanide bridged ligands with nonlinear ∠Mn−N−C of 152.7° and 153.4° have been observed for $A[(Me_3tacn)_6MnCr_6(CN)_{18}](ClO_4)_3$ (A = Na, K; Me_3tacn = *N*,*N*′,*N*″-trimethyl-1,4,7-triazacyclononane) also possessing high-spin Mn^{II}.[13a] Likewise, Zn−N−C angles ranging from 151.4° and 165.1° have been reported for $Zn_3[M^{III}(CN)_6]_2$ (M = Fe, Co), $Zn_3A_2[Fe^{II}(CN)_6]_2$ (A = Rb^+, NH_4^+) possessing ionic Zn^{II},[13b] and an even further reduced ∠Cu^{II}−N−C of 120.1° has been documented.[13c]

Comparison of the $A_2Mn^{II}[Mn^{II}(CN)_6]$ (A = Na, K, Rb, Cs) Structures. Dehydration of **1·H₂O** to **1** leads to a 19% decrease in volume per Mn, and significant structural change from a monoclinic unit cell to rhombohedral unit cell. These structures are unusual as they differ from the well-known fcc Prussian blue motif,[11e] but are related to the recently reported monoclinic $A_2Mn^{II}[Mn^{II}(CN)_6]$ (A = K, Rb).[4] The biggest changes occur for the ∠MnCN and more so for the ∠MnNC angles that deviate from linearity, Table 2. This buckles the structure lowering the symmetry from cubic, as observed for fcc $Cs_2Mn^{II}[Mn^{II}(CN)_6]$ (Figures 6a and 7a), to monoclinic for **1·H₂O** (Figures 6b and 7b), and to rhombohedral for **1** (Figures 6c and 7c). This leads to a shortening of the Mn···Mn separations for the anhydrous compounds by 5% from 5.30 Å for M = Cs to 4.99 Å for M = Na. Hydrated **1·H₂O**, although having nonlinear ∠MnCN and ∠MnNC angles, has a Mn···Mn separation comparable to that for $Cs_2Mn^{II}[Mn^{II}(CN)_6]$.

The structural motif for **1·H₂O** is a consequence of its monoclinic unit cell, as occurs for $A_2Mn^{II}[Mn^{II}(CN)_6]$ (A = K, Rb).[4] Views of the monoclinic **1·H₂O** and rhombohedral **1** structures are shown in Figures 6 and 7. The monoclinic motif is related to the classic Prussian blue translation, *a*, such that the unit cell dimensions are approximately a, $a/\sqrt{2}$, $a/\sqrt{2}$, $\beta \approx 90°$, while the rhombohedral unit cell has dimensions that are approximately $a/\sqrt{2}$, $a/\sqrt{2}$, $a\sqrt{3}$.

Magnetic Properties. The magnetic susceptibilities, $\chi(T)$, of **1** and **1·H₂O** were measured between 5 and 300 K, and are plotted as $\chi T(T)$ and $\chi^{-1}(T)$, Figure 8, and the results are summarized in Table 3.

$Na_2Mn^{II}[Mn^{II}(CN)_6]$ (1). The 300 K value of χT for **1** is 4.54 emuK/mol, which is reduced from the 4.75 emuK/mol expected for the spin-only value for one low- and one high-spin Mn(II) site. This is attributed to strong antiferromagnetic coupling. Upon cooling **1**, $\chi T(T)$ gradually decreases reaching a shallow minima at ∼140 K, which is characteristic of ferrimagnets, before rising abruptly to 106 emu·K/mol at 54 K, suggestive of magnetic ordering. Above 170 K, $\chi^{-1}(T)$ is linear and can be extrapolated to the Curie−Weiss intercept, θ, of −32 K. The $\chi^{-1}(T)$ data can be fit to the Curie−Weiss expression, $\chi \propto (T - \theta)^{-1}$, above ∼130 K with $\theta = -20$ K, and $g = 2$, Figure 8. Hence, above ∼130 K, the Mn^{II} ions in **1** can be considered as being weakly coupled isolated spins. Because of its 3-D extended network structure, this is unexpected, and this may be coincidental.

A fit of the $\chi^{-1}(T)$ data to the Néel hyperbolic equation, eq 1[15] (Figure 8b), gives a T_c of 57 K and θ, θ', and ζ of −35 K, 48 K, and 215 mol K/emu, respectively, for **1**.

$$\chi^{-1} = \frac{T - \theta}{C} - \frac{\zeta}{T - \theta'} \quad (1)$$

The field-cooled (FC) and zero-field-cooled (ZFC) magnetizations for **1** were measured in a 5 Oe magnetic field (Figure 9). The bifurcation temperature, T_b, of the FC/ZFC magnetizations is 59 K for **1**. The remnant, $M_r(T)$, and FC magnetizations are essentially coincident, and extrapolation of the linear $M(T)$ data to zero gives T_c values of 58 and 61 K, respectively.

The 5 K field dependence of the magnetization, $M(H)$, shows an increase with increasing field, H, with respect to the expectation from the Brillouin expression, is suggestive of magnetic ordering for **1** (Figure 10). The 90 kOe magnetization at 5 K is 15 740 emu·Oe/mol for **1**, but is still gradually rising with increasing field. Hence, they are in accord with the expectation of 22 340 emu·Oe/mol for antiferromagnetic coupling leading to ferrimagnetic ordering and are consistent with the reported 70 kOe magnetization at 4.5 K of 24 000 emu·Oe/mol for $K_2Mn[Mn(CN)_6]$.[4] At 5 K, the remanant magnetization, M_r, is 9075 emu·Oe/mol, and the coercive field, H_{cr}, is 15 300 Oe for **1** (Figure 10).

Absorptions in both the frequency-independent in-phase, $\chi'(T)$, and out-of-phase, $\chi''(T)$, components of the AC susceptibility for **1** occur and are characteristic of ferri- or ferromagnetic ordering, Figure 11. The maximum in the 33 Hz $\chi'(T)$ and onset of the $\chi''(T)$ data occur at 58 and 60 K, respectively, for **1**.

The T_c for **1** was determined to be 57, 58, 61, 59, 58, and 60 K from the fit of the $\chi^{-1}(T)$ data to eq 1, the temperatures at which the extrapolation of the M_r and ZFC to zero occurs, the bifurcation temperature, T_b, the temperature at which the peak in $\chi'(T)$ occurs, and the temperature onset upon cooling of

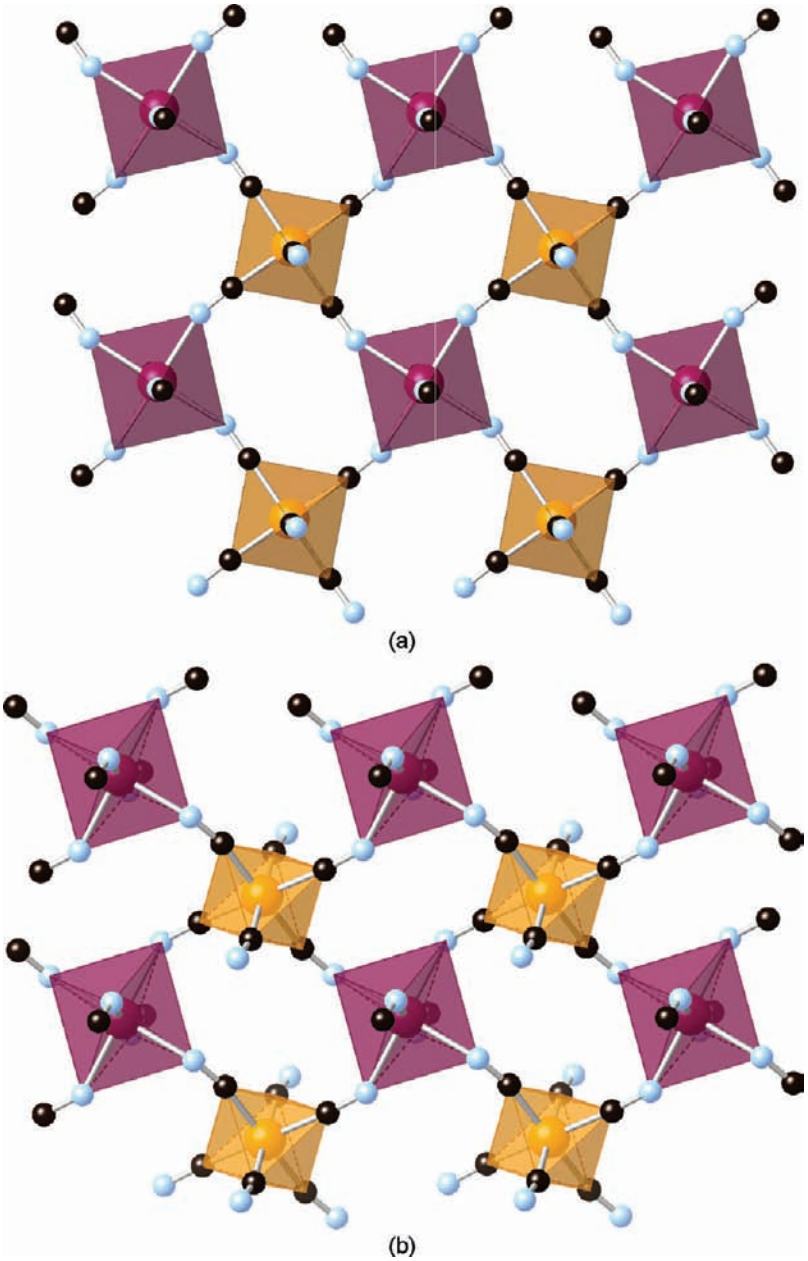

Figure 4. View normal to the *bc* plane of the 3-D network lattice for **1·H$_2$O** (a) and **1** (b), showing MnC_6 surrounded by four MnN_6 octahedra (and vice versa) twisting with respect to each other (Na^+ and H_2O for **1·H$_2$O** are not shown for clarity). [Low-spin (S = 1/2) Mn^{II} is orange; high-spin (S = 5/2) Mn^{II} is maroon; C is black; and N is light blue.]

$\chi''(T)$, respectively. Thus, averaging these temperatures results in a 59 K T_c.

$Na_2Mn^{II}[Mn^{II}(CN)_6]\cdot 2H_2O$ (1·H$_2$O). The 300 K value of χT for **1·H$_2$O** is 5.15 emu·K/mol, which exceeds the 4.75 emu·K/mol expected for the spin-only value for one low- and one high-spin Mn(II) site, Figure 8a. This again is indicative of an anisotropic orbital contribution from the low-spin Mn(II), and the differing average orientations of the polycrystalline samples. Upon cooling **1·H$_2$O**, $\chi T(T)$ decreases and reaches a minima at ~36 K that is characteristic of a ferrimagnet, before rising abruptly to 5.8 emu·K/mol at 21 K suggestive of magnetic ordering. A peak is also present at 56 K that is attributed to a small amount of **1**. On the basis of the amplitude of the peak for **1·H$_2$O** with respect to that occurring for **1** (Figure 8a), ~0.4% **1** is present in **1·H$_2$O**. For **1·H$_2$O**, above 57 K, the $\chi^{-1}(T)$ is linear whose line extrapolates to an intercept of θ = −33 K, and only a poor fit to the Curie−Weiss expression with θ = −23 K, and g = 2 for the high-spin Mn^{II} site, but g = 3.3 for the high-spin Mn^{II} site, and a TIP of 150 × 10^{-6} emu/mol, Figure 8b. Hence, **1·H$_2$O** cannot be well described as weakly coupled isolated spins in accord with its 3-D extended network structure. As noted above, it is unexpected in contrast that **1** can be modeled by the Curie−Weiss expression above ~130 K due to its 3-D extended network structure, but this may be coincidental.

The significant negative θ value indicates significant antiferromagnetic couplings, and the increases in $\chi T(T)$ at low temperature suggest the onset of magnetic ordering. Unlike for **1**, fitting of the $\chi^{-1}(T)$ data to eq 1 was unsuccessful for **1·H$_2$O** presumably due to the presence to **1**.

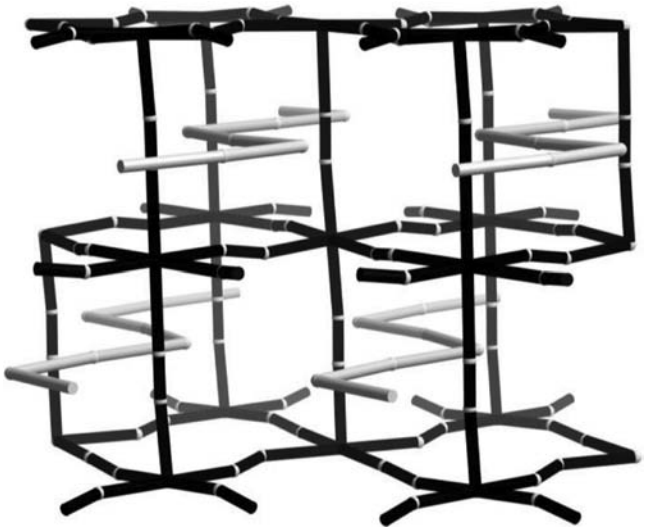

Figure 5. 1-D zigzag Na−O chains (gray) interpenetrating the 3-D $Mn[Mn(CN)_6]$ lattice (black).

Table 2. Average Room-Temperature $Mn^{II}\cdots Mn^{II}$ Distances, ∠MnCN, and ∠MnNC for $1\cdot H_2O$, 1, and $A_2Mn^{II}[Mn^{II}(CN)_6]$ (A = K, Rb, Cs)[4]

compound	∠MnCN, deg	∠MnNC, deg	Mn···Mn, Å
$Na_2Mn^{II}[Mn^{II}(CN)_6]\cdot 2H_2O$ ($\mathbf{1\cdot H_2O}$)	176.1	165.3	5.33
$Na_2Mn^{II}[Mn^{II}(CN)_6]$ (**1**)	167.0	142.4	4.99
$K_2Mn^{II}[Mn^{II}(CN)_6]$	173.2	148.8	5.09
$Rb_2Mn^{II}[Mn^{II}(CN)_6]$	177.2	153.3	5.19
$Cs_2Mn^{II}[Mn^{II}(CN)_6]$	180	180	5.30

The field-cooled (FC) and zero-field-cooled (ZFC) magnetizations for $\mathbf{1\cdot H_2O}$ were measured in a 5 Oe magnetic field (Figure 12). As occurs for **1**, the $M_r(T)$ and FC magnetizations are coincident, and extrapolation of the linear $M(T)$ data a $M(T) \rightarrow 0$ gives T_c of 31 K for each. A bifurcation temperature, T_b, of the FC/ZFC magnetizations, however, is not observed due to the presence of **1**, but is estimated to be ∼30 K for $\mathbf{1\cdot H_2O}$. To again estimate the amount of **1** present as an impurity, as the magnetization at 33 K is attributed to **1**, its value with respect to that expected for a pure sample of **1** (Figure 9) provides an estimate of ∼0.8% for **1** as an impurity in $\mathbf{1\cdot H_2O}$, in accord with the aforementioned estimate of 0.4% from the $\chi T(T)$ data.

The 5 K field dependence of the magnetization, $M(H)$, shows an almost linear increase with increasing field, H, for $\mathbf{1\cdot H_2O}$ (Figure 13) with the 90 kOe magnetizations at 5 K of 8630 emu·Oe/mol for **1**, but rising with increasing field without evidence of saturation. Although far from saturation, this low value suggests antiferromagnetic coupling leading to ferrimagnetic ordering. At 5 K, the remnant magnetization, M_r, is 120 emu·Oe/mol, and the coercive field, H_c, is 850 Oe for $\mathbf{1\cdot H_2O}$.

Frequency-independent absorptions in both $\chi'(T)$ and $\chi''(T)$ for $\mathbf{1\cdot H_2O}$ occur and are characteristic of ferri- or ferromagnetic ordering, Figure 14. The maxima in the 33 Hz $\chi'(T)$ and onset of the peak in $\chi''(T)$ occur at 29 and 31 K for $\mathbf{1\cdot H_2O}$, respectively.

The T_c for $\mathbf{1\cdot H_2O}$ was determined to be 31, 31, 30, 29, and 31 K from the temperatures at which the extrapolation of the M_r and ZFC to zero occurs, the bifurcation temperature, T_b, the temperature at which the peak in $\chi\cdot(T)$ occurs, and the temperature onset upon cooling of $\chi''(T)$, respectively. Thus, averaging these temperatures results in a T_c of 30 K.

Comparison of the Magnetic Properties of $A_2Mn[Mn(CN)_6]$ (A = Na, Na·2H_2O, K, Rb, Cs). The PBAs of the

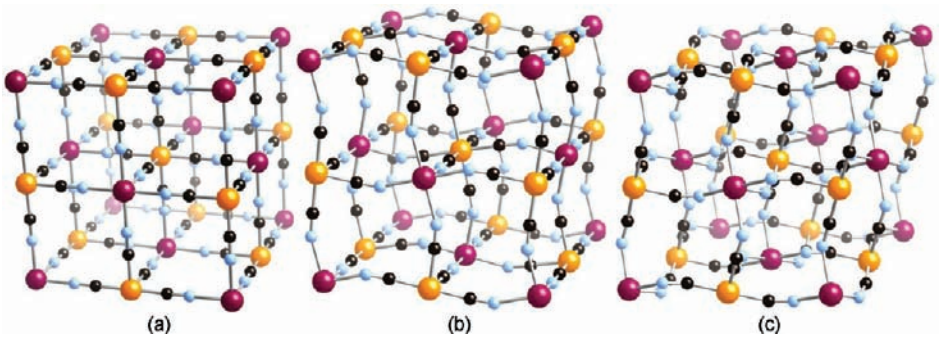

Figure 6. Perspective view of *fcc* $Cs_2Mn^{II}[Mn^{II}(CN)_6]$ (a), monoclinic $\mathbf{1\cdot H_2O}$ (b), and rhombohedral **1** (c). The cations are not shown for clarity. [Low-spin (S = 1/2) Mn^{II} is orange; high-spin (S = 5/2) Mn^{II} is maroon; C is black; and N is light blue.]

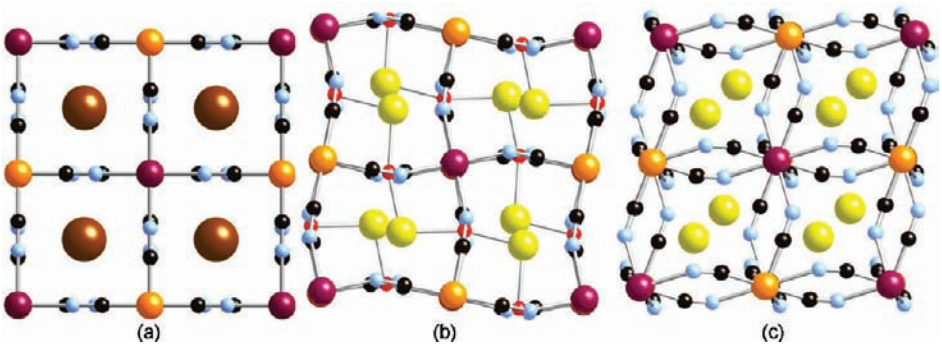

Figure 7. View along the *a*-axis for *fcc* $Cs_2Mn^{II}[Mn^{II}(CN)_6]$ (a), monoclinic $\mathbf{1\cdot H_2O}$ (b), and rhombohedral **1** (c) showing the location of the respective cations. [Low-spin (S = 1/2) Mn^{II} is orange; high-spin (S = 5/2) Mn^{II} is maroon; Cs is brown, O is red; Na is yellow; C is black; and N is light blue.]

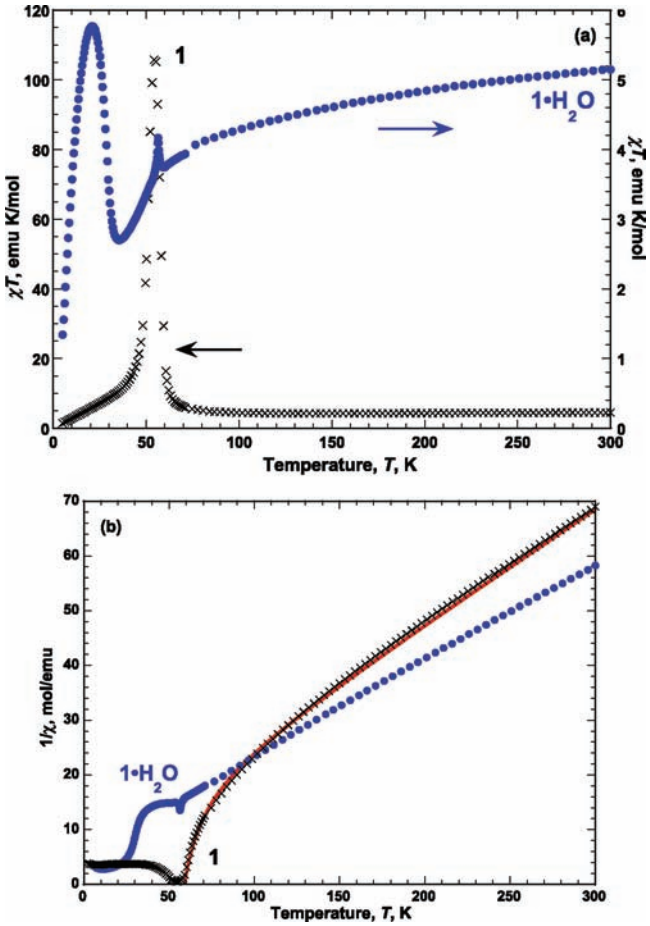

Figure 8. $\chi T(T)$ (a) and $\chi^{-1}(T)$ (b) for **1** (×) and **1·H$_2$O** (●). The solid line (−) in $\chi^{-1}(T)$ represents the best fit to the Néel hyperbolic equation, eq 1.

composition $A_2Mn[Mn(CN)_6]$ (A = Na, Na·2H$_2$O, K, Rb, Cs) exhibit an increasing deviation of linearity of the Mn−N≡C linkages [142.4° (Na^+) > 148.8° (K^+) > 153.3° (Rb^+) > 165.3°

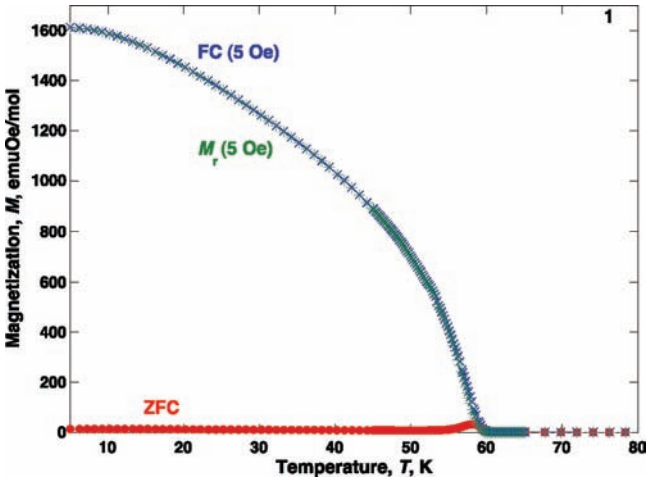

Figure 9. Field-cooled (×), zero-field-cooled (●), and remnant magnetization (+), $M_r(T)$, for **1** showing the bifurcation temperature, T_b, at 59 K.

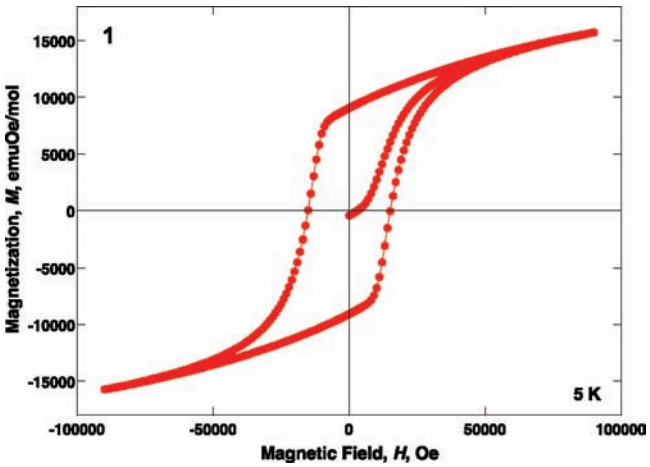

Figure 10. $M(H)$ for **1** (●).

Table 3. Summary of Magnetic Properties for 1 and 1·H$_2$O, and Comparison to $A_2Mn[Mn(CN)_6]$ (A = K, Rb, Cs)

	A						
	K^{+a}	K^{+b}	K^+	Rb^+	Cs^+	Na^+ (**1**)	Na^+ (**1**·H$_2$O)
$\chi_{obs}T$, emu·K/mol (295 K)	5.56	5.10	4.99	4.83	4.68	4.54	5.15
$\chi_{calc}T$, emu·K/mol (spin-only)	4.75	4.75	4.75	4.75	4.75	4.75	4.75
T_{min}, K	90	105	105	100	26	140	36
θ, K $\chi^{-1}(T) \rightarrow 0]^c$	−60	−65	−19	−30	−15	−32	−33
θ, K [Curie−Weiss; $\chi \propto (T-\theta)^{-1}$]	*d*	*d*	*d*	*d*	*d*	−20	
θ, K (Néel), eq 1	−33	−20	*d*	−19	−15	−35	*e*
θ', K (Néel), eq 1	35	35.5	*d*	27		48	*e*
T_N, K (Néel), eq 1	41	41	41	34.6	21	57	*e*
T_c, K ($M_r \rightarrow 0$)	*d*	*d*	42	35	*d*	58	31
T_c, K ($M_{ZFC} \rightarrow 0$)	42	42	*d*	37	23	61	31
T_b, K (ZFC/FC)	47	46	*d*	38	24	59	∼30
T_p, K (ac) from $\chi'(T)$ (33 Hz)	38	38	*d*	34	22	58	29
T_c, K (ac) from onset of $\chi''(T)$ (33 Hz)	46	44	*d*	37	24	60	31
H_{cr}, Oe	3900	9150	370[f]	8850	5000	15 300	850
M, emu·Oe/mol (5 K, 50 kOe)	16 100[g]	15 800[g]	24 000[f,h]	16 350[g]	9360[g]	13 300[g,i]	4435[g,j]
M_r, emu·Oe/mol	8600	9350	4900[f]	9300	640	9075	120
ref	4	4	14	4	4	this work	this work

[a]From H$_2$O. [b]From MeOH. [c]Extrapolated from the high temperature linear region of $\chi^{-1}(T)$. [d]Not reported. [e]Not obtained; see text. [f]24 K. [g]Not saturated. [h]70 kOe. [i]15 740 emu·Oe/mol at 90 kOe. [j]8630 emu·Oe/mol at 90 kOe.

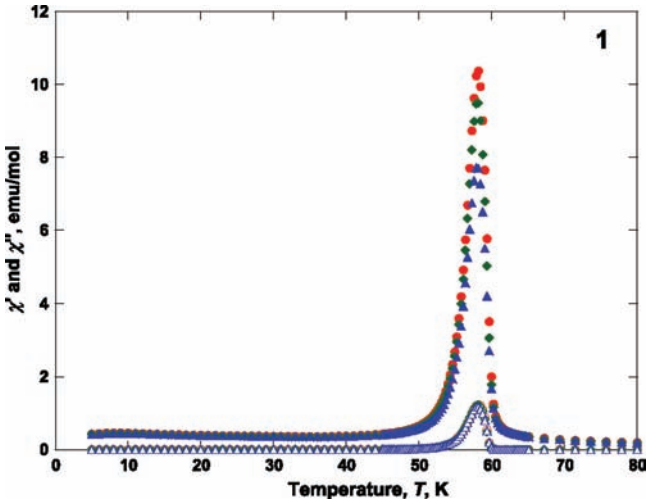

Figure 11. $\chi'(T)$ (filled symbols) and $\chi''(T)$ (open symbols) for **1** at 33 (●, ○), 100 (◆, ◇), and 1000 Hz (▲, △).

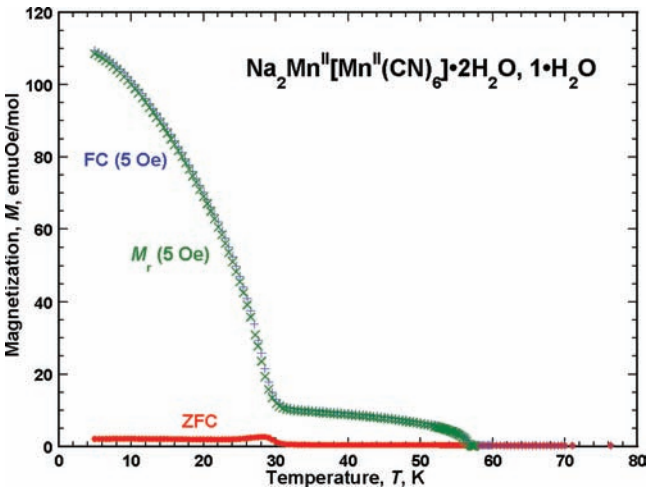

Figure 12. Field-cooled (×), zero-field cooled (●), and remnant magnetization (+), $M_r(T)$, for **1·H$_2$O**.

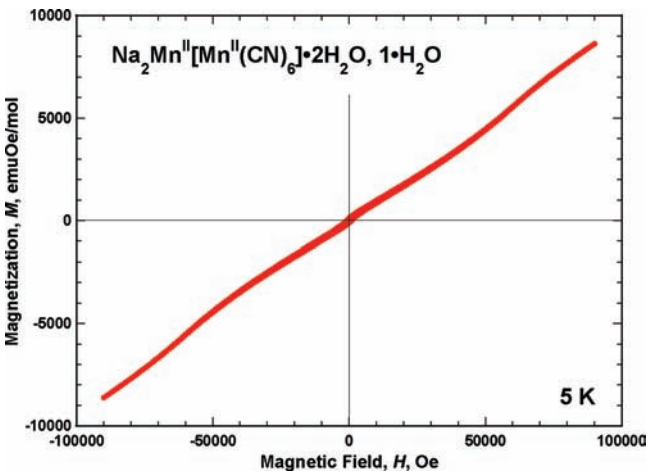

Figure 13. $M(H)$ for **1·H$_2$O** (●).

(Na^+·$2H_2O$) > 180° (Cs^+)] and a concomitant increase in T_c [59 K (Na^+) > 41 K (K^+) > 34.6 K (Rb^+) > 30 K (Na^+·$2H_2O$) > 21 K (Cs^+)]. In contrast, the coercivity, H_{cr} [15 300 Oe (Na^+) > 9150 Oe (K^+, from MeOH) > 8850 Oe (Rb^+) > 5000

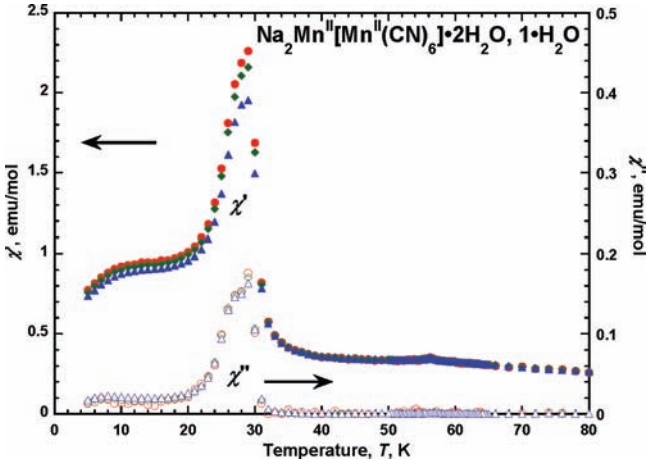

Figure 14. $\chi'(T)$ (filled symbols) and $\chi''(T)$ (open symbols) for **1·H$_2$O** at 33 (●, ○), 100 (◆, ◇), and 1000 Hz (▲, △).

Oe (Cs^+) > 3900 Oe (K^+, from H_2O) > 850 Oe (Na^+·$2H_2O$)], of these PBAs does not follow the same trend as T_c and, in the case of the $K_2Mn[Mn(CN)_6]$, is dependent on the synthetic route. Also, the remnant magnetizations, $M_r(T)$, and the 5 K field-dependent magnetizations, $M(H)$ (Table 3), do not follow a direct trend relative to the increasing deviation of linearity of the Mn−N≡C linkages. Interestingly, the hydrated sodium analogue, **1·H$_2$O**, has $M_r(T)$ and $M(H)$ values, which are reduced from the Cs analogue even though **1·H$_2$O** has reduced Mn−N≡C dihedral angles.

■ CONCLUSION

$Na_2Mn[Mn(CN)_6]$ (**1**) and $Na_2Mn[Mn(CN)_6]\cdot 2H_2O$ (**1·H$_2$O**) along with $K_2Mn[Mn(CN)_6]$ and $Rb_2Mn[Mn(CN)_6]$ are the only known non-*fcc* materials of Prussian blue composition. All, including *fcc* $Cs_2Mn[Mn(CN)_6]$, are composed of low-spin (S = 1/2) $Mn^{II}C_6$ octahedra adjacent to high-spin (S = 5/2) $Mn^{II}N_6$ octahedra forming a 3-D extended network structure that orders as a ferrimagnet. While the ∠Mn−C−N angles are linear, ∠Mn−N−C angles deviate significantly from linearity, and the greater is the deviation, the greater is the T_c, Figure 15. The significant ionic character (less directional

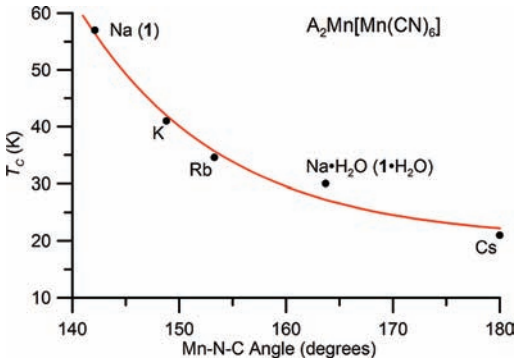

Figure 15. Correlation of increasing T_N with deviation from linearity of the ∠Mn−N−C for $A_2Mn^{II}[Mn^{II}(CN)_6]$ (A = Na, K, Rb, Cs). The line is a general guide for the eye.

covalency) associated with Mn^{II12} accommodates the significantly reduced ∠Mn−N−C that is observed. Thus, the bent cyanide Mn−N−C bridges play a crucial role in the

superexchange mechanism by increasing the coupling via shorter Mn(II)···Mn(II) separations, and perhaps an enhanced overlap.

■ ASSOCIATED CONTENT

Supporting Information

Powder X-ray crystallographic information files (CIF) for **1** and **1·H_2O** at room temperature and at 16 K (CCDC 848211, 848212, and 848213, respectively), and the fractional coordinates of the atoms in the asymmetric unit of **1·H_2O** and **1**. This material is available free of charge via the Internet at http://pubs.acs.org.

■ AUTHOR INFORMATION

Corresponding Author

jsmiller@chem.utah.edu; peter.stephens@sunysb.edu

Present Address

[§]GE Global Research, 1 Research Circle, Niskayuna, New York 12309, United States.

■ ACKNOWLEDGMENTS

We appreciate the continued support by the Department of Energy Division of Material Science (Grant No. DE-FG03-93ER45504), and fitting of the magnetic data to the Neél equation by Amber C. McConnell. Use of the National Synchrotron Light Source, Brookhaven National Laboratory, was supported by the U.S. Department of Energy, Office of Basic Energy Sciences, under Contract No. DE-AC02-98CH10886.

■ REFERENCES

(1) Verdaguer, M.; Girolami, G. S. In *Magnetism – Molecules to Materials*; Miller, J. S., Drillon, M., Eds.; Wiley-VCH: Weinheim, 2005; Vol. *5*, p 283. Hashimoto, K.; Ohkoshi, S. *Philos. Trans. R. Soc., A* **1999**, *357*, 2977. Verdaguer, M.; Bleuzen, A.; Marvaud, V.; Vaissermann, J.; Seuleiman, M.; Desplanches, C.; Scuiller, A.; Train, C.; Garde, R.; Gelly, G.; Lomenech, C.; Rosenman, I.; Veillet, P.; Cartier, C.; Villain, F. *Coord. Chem. Rev.* **1999**, *190–192*, 1023.

(2) (a) Ferlay, S.; Mallah, T.; Ouahes, R.; Veillet, P.; Verdaguer, M. *Nature* **1995**, *378*, 701. (b) Dujardin, E.; Ferlay, S.; Phan, X.; Desplanches, C.; Moulin, C. C. D.; Sainctavit, P.; Baudelet, F.; Dartyge, E.; Veillet, P.; Verdaguer, M. *J. Am. Chem. Soc.* **1998**, *120*, 11347. (c) Ferlay, S.; Mallah, T.; Ouahes, R.; Veillet, P.; Verdaguer, M. *Inorg. Chem.* **1999**, *38*, 229. (d) Verdaguer, M.; Bleuzen, A.; Train, C.; Garde, R.; Fabrizi de Biani, F.; Desplanches, C. *Philos. Trans. R. Soc., A* **1999**, *357*, 2959.

(3) (a) Holmes, S. M.; Girolami, G. S. *J. Am. Chem. Soc.* **1999**, *121*, 5593. (b) Hatlevik, Ø.; Buschmann, W. E.; Zhang, J.; Manson, J. L.; Miller, J. S. *Adv. Mater.* **1999**, *11*, 914.

(4) Her, J.-H.; Stephens, P. W.; Kareis, C. M.; Moore, J. G.; Min, K. S.; Park, J.-W.; Bali, G.; Kennon, B. S.; Miller, J. S. *Inorg. Chem.* **2010**, *49*, 1524.

(5) (a) Anderson, P. W. *Phys. Rev.* **1950**, *79*, 350. (b) Goodenough, J. B. *J. Phys. Chem. Solids* **1958**, *6*, 287. (c) Kanamori, J. *J. Phys. Chem. Solids* **1959**, *10*, 87.

(6) Brandon, E. J.; Rittenberg, D. K.; Arif, A. M.; Miller, J. S. *Inorg. Chem.* **1998**, *37*, 3376.

(7) Bruker AXS. *TOPAS V4: General Profile and Structure Analysis Software for Powder Diffraction Data-User's Manual*; Bruker AXS: Karlsruhe, Germany, 2005.

(8) (a) Coelho, A. A. *J. Appl. Crystallogr.* **2000**, *33*, 899. (b) Coelho, A. A. *J. Appl. Crystallogr.* **2003**, *36*, 86.

(9) TOPAS-Academic is available at http://www.topas-academic.net.

(10) (a) Matecki, G.; Ratuszna, A. *Powder Diffr.* **1999**, *14*, 25. (b) Matsuda, T.; Kim, J.; Moritomo, Y. *J. Am. Chem. Soc.* **2010**, *132*, 12206.

(11) (a) Tullberg, A.; Vannerberg, N. *Acta Chem. Scand., Ser. A* **1974**, *28*, 551. (b) Tullberg, A.; Vannerberg, N.-G. *Acta Chem. Scand.* **1971**, *25*, 343. (c) Beall, G. W.; Milligan, W. O.; Korp, J.; Bernal, I. *Inorg. Chem.* **1977**, *16*, 2715. (d) Brown, D. B.; Shriver, D. F. *Inorg. Chem.* **1969**, *8*, 37. (e) Ludi, A.; Güdel, H. U. *Struct. Bonding (Berlin)* **1973**, *14*, 1.

(12) Covalency increases with crystal field stabilization, Δ_o; hence, high-spin $Mn^{II}N_6$ is more ionic than low-spin $Mn^{II}C_6$. Mingos, D. M. P. *Essential Trends in Inorganic Chemistry*; Oxford University Press: New York, 1998; p 331.

(13) (a) Heinrich, J. L.; Sokol, J. J.; Hee, A. G.; Long, J. R. *J. Solid State Chem.* **2001**, *159*, 293. (b) Rodríquez-Hernández, J.; Reguera, E.; Lima, E.; Balmaseda, J.; Martínez-Garcia, R.; Yee-Maderia, H. *J. Phys. Chem. Solids* **2007**, *68*, 1630. (c) Escorihuela, I.; Falvello, L. R.; Tomás, M. *Inorg. Chem.* **2001**, *40*, 636.

(14) (a) Entley, W. R.; Girolami, S. G. *Inorg. Chem.* **1994**, *33*, 5165. (b) Entley, W. R.; Girolami, S. G. *Inorg. Chem.* **1995**, *34*, 2262.

(15) (a) Néel, L. *Ann. Phys.* **1948**, *3*, 137. (b) Smart, J. S. *Am. J. Phys.* **1955**, *23*, 356.